PROCEEDINGS OF SCIENCE

Lattice QCD calculation of the pion generalized parton distribution

Heng-Tong Ding,[a] **Xiang Gao,**[b] **Swagato Mukherjee,**[c] **Peter Petreczky,**[c] **Qi Shi,**[a,c,*] **Sergey Syritsyn**[d,e] **and Yong Zhao**[b]

[a] *Key Laboratory of Quark and Lepton Physics (MOE) and Institute of Particle Physics, Central China Normal University, Wuhan 430079, China*

[b] *Physics Division, Argonne National Laboratory, Lemont, Illinois 60439, USA*

[c] *Physics Department, Brookhaven National Laboratory, Bldg. 510A, Upton, New York 11973, USA*

[d] *RIKEN-BNL Research Center, Brookhaven National Laboratory, Upton, New York 11973, USA*

[e] *Department of Physics and Astronomy, Stony Brook University, Stony Brook, New York 11790, USA*

E-mail: qshi1@bnl.gov

We present the results of a Lattice QCD computation of pion generalized parton distribution (GPD), employing perturbative matching up to next-to-next-to-leading order (NNLO). The computations are based on an ensemble of $N_f = 2 + 1$ highly improved staggered quarks (HISQ) with a pion mass of 300 MeV and a lattice spacing of 0.04 fm. Centered on the zero-skewness limit, we utilize a recently proposed Lorentz-invariant definition of GPD, which is derived from Lorentz-invariant amplitudes. We analyze and compare these amplitudes in both Breit and non-Breit kinematic frames at comparable momentum transfers, validating their frame-independent nature. To obtain light-cone GPD, we integrate hybrid scheme renormalization with the large momentum effective theory (LaMET). Moreover, we determine the first three iso-vector generalized form factors (GFFs) of the pion using the ratio scheme renormalization and leading-twist factorization, achieving NNLO accuracy.

25th International Spin Physics Symposium (SPIN 2023)
24-29 September 2023
Durham, NC, USA

*Speaker

PoS(SPIN2023)024

1. Introduction

Since its discovery in 1947, the pion has been the subject of intense research, recognized for its dual identity as both a Goldstone boson linked to chiral symmetry breaking and a QCD-bound state. Over the years, substantial efforts have been dedicated to studying its internal structure by analyzing experimental data. Key methodologies have involved extracting form factors (FFs) through pion-electron scattering [1] and discerning parton distribution functions (PDFs) via the Drell-Yan process [2]. However, these approaches are limited to revealing only the one-dimensional structure of the hadron. For a more comprehensive, three-dimensional perspective, the focus has shifted to GPD, a concept introduced in the 1990s [3–6]. Access to GPD is typically gained through exclusive reactions, notably deeply virtual Compton scattering (DVCS) and deeply virtual meson production (DVMP).

Presently, a series of experiments are being conducted or planned, which can enrich our comprehension of pion particles. Prominent among these are the JLab 12-GeV program [7], the Apparatus for Meson and Baryon Experimental Research (AMBER) at CERN SPS [8], the forthcoming Electron-Ion Collider (EIC) at Brookhaven National Laboratory [9], and the Electron-Ion Collider in China (EicC) [10]. These initiatives are designed to probe the pion at various energy levels. However, extracting GPD from experimental data is fraught with challenges, including the chiral-odd nature of certain distributions and the complexity involved in pion production. On the other hand, lattice QCD results, offering supplementary insights and potentially guiding experimental efforts, are highly sought after. The advent of Large-Momentum Effective Theory (LaMET) in 2013 [11] marked a pivotal shift, extending GPD studies beyond just the first few Mellin moments. This spurred a flurry of lattice-based research on nucleon and meson structures utilizing LaMET, and please refer to, e.g., Ref. [12] for a recent review.

While there are several lattice QCD studies of the nucleon GPD, pion GPD has been explored so far by only one lattice group [13, 14]. Traditionally, calculations are conducted in the Breit frame, requiring the momentum transfer to be symmetrically distributed between the initial and final states. This approach incurs substantial computational costs. However, a recent breakthrough has been achieved with the introduction of a frame-independent method for lattice GPD calculations [15]. This innovative approach holds the potential to significantly reduce computational expenses.

In this study, we present our lattice calculations of the pion GPD using the LaMET approach, featuring a refined lattice spacing of 0.04 fm within the non-Breit frame. Additionally, we calculate the first three iso-vector GFFs utilizing the leading-twist Operator Product Expansion (OPE). The organization of this proceeding is as follows: In Section 2, we outline our lattice setup and describe the methodologies employed to extract the bare matrix elements from the combined analysis of two- and three-point correlation functions. Section 3 focuses on validating the frame-independent approach by analyzing lattice data obtained from both Breit and non-Breit frames, which have comparable momentum transfer values. This analysis enables us to perform calculations in an asymmetric kinematic setting. In Section 4, we detail the renormalization process of the bare matrix elements using the hybrid scheme and subsequently apply LaMET matching to derive the valence GPD. Furthermore, in Section 5, we discuss the renormalization of matrix elements at short distances using the ratio scheme, followed by the extraction of the GFF through leading-twist factorization. Finally, Section 6 provides a summary of our findings and offers an outlook on future

research directions.

2. Lattice calculation

2.1 Lattice setup

Our lattice calculations use the gauge ensembles provided by the HotQCD collaboration [16], utilizing a 2+1 flavor setup with Highly Improved Staggered Quark (HISQ) action [17]. The lattice configuration has dimensions of $N_s \times N_t = 64^3 \times 64$ and a lattice spacing of $a = 0.04$ fm. The sea quark masses are adjusted to yield a pion mass of 160 MeV. In the valence sector, we use the Wilson-Clover action with 1 level of hypercubic (HYP) smearing [18]. For the coefficient of the clover term, we use the tree-level tadpole improved value using the fourth root of the plaquete resulting in 1.02868 [19]. The valence quark masses in the Wilson-Clover action are tuned to $am_q = -0.033$, resulting in a pion mass of 300 MeV.

Central to our computational approach is the use of momentum-boosted smeared sources [20]. The quark propagators are obtained through the application of the multigrid algorithm [21] to invert the Wilson-Dirac operator using the QUDA software suite [22–24] on GPUs. The periodic boundary condition determines the spatial momentum defined in lattice units as $P_z = 2\pi n_z/(aN_s)$ with n_z being an integer. In our approach, the momentum-boosted sources and sinks are constructed with a Gaussian profile with boost momenta $k_z = 2\pi m_z/(aN_s)$ in the z-direction. Source construction is done in the Coulomb gauge, and the Gaussian profile is created with the radius of 0.208 fm [19, 25]. Employing these quark propagators, we have computed both two-point and three-point hadron correlation functions. To increase statistics per configuration, we combined multiple exact (high-precision) and sloppy (low-precision) samples and implemented the all-mode averaging (AMA) technique [26]. The lattice parameters used in this study are summarized in Table 1. In the limit of zero-skewness ($\xi = 0$), there is no momentum transfer in the z-direction.

Table 1: The information about the lattice parameters used in two different kinematic frames are shown. The symbol t_s represents the source-sink separation. We present the momentum in units of $2\pi/N_s/a$, including the final momentum ($\mathbf{n}^f$), the boost momentum along z-direction (m_z), and the momentum transfer ($\mathbf{n}^q = \mathbf{n}^f - \mathbf{n}^i$) where $\mathbf{n}^i$ denotes the initial momentum. Additionally, we provide the total number of gauge configurations (#cfgs) as well as the counts for both exact (#ex) and sloppy (#sl) inversion samples per configuration.

Frame	t_s/a	$\mathbf{n}^f = (n_x^f, n_y^f, n_z^f)$	m_z	$\mathbf{n}^q = (n_x^q, n_y^q, n_z^q)$	#cfgs	(#ex, #sl)
Breit	9,12,15,18	(1, 0, 2)	2	(2, 0, 0)	115	(1, 32)
non-Breit	9,12,15,18	(0,0,0)	0	[(0,0,0), (1,0,0) (1,1,0), (2,0,0) (2,1,0), (2,2,0)]	314	(3, 96)
	9,12,15,18	(0,0,1)	0		314	(3, 96)
	9,12,15,18	(0,0,2)	2		314	(4, 128)
	9,12,15	(0,0,3)	2		314	(4, 128)
	9,12,15	(0,0,4)	3		564	(4, 128)

2.2 Correlation functions

To obtain the bare matrix elements, it is necessary to compute two- and three-point correlation functions. The two-point correlation function is defined as

$$C_{2\text{pt}}(\mathbf{P}, t_s) = \sum_{\mathbf{x}} e^{-i\mathbf{P}\cdot\mathbf{x}} \left\langle \pi_s(\mathbf{x}, t_s)\pi_s^\dagger(\mathbf{0}, 0)\right\rangle, \tag{1}$$

where $\mathbf{P}$ denotes the spatial momentum, $\mathbf{x}$ and $\mathbf{0}$ represent the spatial coordinates, and t_s and 0 correspond to the time coordinates. Here $\pi_s^\dagger$ and π_s, stands for the pion creation and annihilation operators, respectively, and the subscript s indicates smeared operators.

The three-point correlation function is defined as

$$C_{3\text{pt}}(\mathbf{P}^f, \mathbf{q}; t_s, \tau; z) = \sum_{\mathbf{x},\mathbf{y}} e^{-i\mathbf{P}^f\cdot\mathbf{x}} e^{i\mathbf{q}\cdot\mathbf{y}} \left\langle \pi_s(\mathbf{x}, t_s) O_{\gamma_t}(\mathbf{y}, \tau; z)\pi_s^\dagger(\mathbf{0}, 0)\right\rangle, \tag{2}$$

where $\mathbf{P}^f$ and $\mathbf{q}$ denote the final momentum and momentum transfer, respectively. The initial momentum can be expressed as $\mathbf{P}^i = \mathbf{P}^f - \mathbf{q}$. The quark bilinear operator is symbolized by O_{γ_t} and is characterized by its spacetime insertion position, indicated by coordinates $(\mathbf{y}, \tau)$. This operator is also associated with a Wilson line, which extends along the z-direction for a length of z.

For a comprehensive analysis, it is essential to initially extract the energy and the corresponding amplitude of the particle from the two-point correlation function, which also enables us to assess the quality of our data. The spectral decomposition of the two-point correlation function is

$$C_{2\text{pt}}(\mathbf{P}, t_s) = \sum_{n=0}^{N-1} A_n A_n^* \left[e^{-E_n(\mathbf{P})t_s} + e^{-E_n(\mathbf{P})(aN_t - t_s)} \right], \tag{3}$$

where N denotes the total number of energy levels, E_n and $A_n = \left\langle \Omega|\hat{H}|n\right\rangle$ are the energy and the amplitude of the n-th energy level, and $|\Omega\rangle$ is the vacuum state.

As for the three-point correlation function, its spectral decomposition can be written as

$$C_{3\text{pt}}(\mathbf{P}^f, \mathbf{P}^i; t_s, \tau; z) = \sum_{n,m=0}^{N-1} A_n^f (A_m^i)^* e^{-E_n(\mathbf{P}^f)(t_s-\tau)} e^{-E_m(\mathbf{P}^i)\tau} \times \left\langle n; \mathbf{P}^f|O_{\gamma_t}|m; \mathbf{P}^i\right\rangle. \tag{4}$$

The matrix elements of the ground state, denoted by $\left\langle 0; \mathbf{P}^f|O_{\gamma_t}|0; \mathbf{P}^i\right\rangle$, represent the main quantity required for calculating GPD.

2.3 Bare matrix element

To extract the bare matrix elements, defined as $F^B = 2\sqrt{E_0^f E_0^i}\left\langle 0; \mathbf{P}^f|O_{\gamma_t}|0; \mathbf{P}^i\right\rangle / (E_0^f + E_0^i)$, we construct a ratio that capitalizes on the inherent relationship between the two-point and three-point correlation functions.

$$R(\mathbf{P}^f, \mathbf{P}^i; t_s, \tau; z) \equiv \frac{2\sqrt{E_0^f E_0^i}}{E_0^f + E_0^i} \frac{C_{3\text{pt}}(\mathbf{P}^f, \mathbf{P}^\mathbf{i}; t_s, \tau; z)}{C_{2\text{pt}}(\mathbf{P}^f, t_s)} \times \left[\frac{C_{2\text{pt}}(\mathbf{P}^i, t_s - \tau) C_{2\text{pt}}(\mathbf{P}^f, \tau) C_{2\text{pt}}(\mathbf{P}^f, t_s)}{C_{2\text{pt}}(\mathbf{P}^f, t_s - \tau) C_{2\text{pt}}(\mathbf{P}^i, \tau) C_{2\text{pt}}(\mathbf{P}^i, t_s)} \right]^{1/2}, \tag{5}$$

where E_0^i and E_0^f denote the ground state energy of the initial and final states, respectively. The ratio asymptotically approaches the bare matrix element F^B as t_s tends to infinity. By implementing Eqs. (3) - (5) and utilizing the extracted values of energy and amplitude, we are able to execute a fitting process on the lattice data, which enables us to extract the bare matrix elements.

3. Frame-independent approach

Prior to performing the principal data analysis, it is crucial to introduce the pioneering frame-independent approach for calculating the GPD on the lattice [15]. In this framework, one parametrizes the quasi-GPD (qGPD) matrix elements of the pion in terms of Lorentz-invariant amplitudes, A_i, with appropriate kinematic factors.

$$F^{\mu}(\bar{P}^{\mu}, z^{\mu}, q^{\mu}) = \frac{1}{\sqrt{E_0^i E_0^f}} \left(\bar{P}^{\mu} A_1 + m_{\pi}^2 z^{\mu} A_2 + q^{\mu} A_3 \right), \tag{6}$$

where the superscript $\mu = (t, x, y, z)$ represents the Lorentz indices, $\bar{P} = \left(P^i + P^f\right)/2$ the average of the initial and final energy momenta, $q = P^f - P^i$ the momentum transfer and m_{π} the mass of the pion. Furthermore, z^{μ} denotes the separation between the quark and anti-quark fields. Based on these frame-independent amplitudes, one can get the qGPD by performing the Fourier transform of the Lorentz-invariant definition of (quasi) GPD

$$H_I^{\mu}(\bar{P}^{\mu}, z^{\mu}, q^{\mu}) = A_1 + \frac{z^{\mu} q_{\mu}}{z^{\mu} \bar{P}_{\mu}} A_3. \tag{7}$$

Generally, due to the ultraviolet (UV) divergence induced by the Wilson line, a separated renormalization step is needed before the Fourier transform. Furthermore, by studying the behavior under hermiticity and time-reversal transformations simultaneously, it was found that the amplitude A_3 is an odd function of $z^{\mu} q_{\mu}$ [15]. In this study, considering zero-skewness and $z^{\mu} = (0, 0, 0, z)$, it is expected that A_3 should be equal to 0. Subsequently, we will use lattice data to investigate the frame-independence of the amplitudes and whether the value of A_3 is zero.

For convenience, we will use the expression $Q^2 = -q^2$ to represent the momentum transfer below. The variables F^{μ} presented on the left-hand side of Eq. (6) are the matrix elements, $\left\langle n; \mathbf{P}^f | O_{\gamma_{\mu}} | m; \mathbf{P}^i \right\rangle$, which are calculable on a lattice. Combining lattice results obtained in different kinematics, Eq. (6) enables us to deduce the Lorentz-invariant amplitudes A_i. The results of A_i must be frame-independent and should agree between the Breit and non-Breit frames for comparable Q^2 values. Our analysis involves two sets of lattice data, both at a momentum of $P_z = 0.968$ GeV. These datasets exhibit similar Q^2 values: the dataset from the Breit frame has $Q^2 = 0.938$ GeV^2, while the dataset from the non-Breit frame has $Q^2 = 0.952$ GeV^2. The results shown in Fig. 1 indicate that both A_1 and A_3 amplitudes are consistent between the Breit and non-Breit frames within a reasonable region of z. Notably, the results of A_3 in both frames are compatible with zero up to statistical fluctuations. These findings validate the correctness of the frame-independent approach. In our case, the Lorentz-invariant (quasi) GPD H_I equals the amplitude A_1. Specifically, the time component of H_I directly corresponds to the bare matrix element F^B:

$$H_I^t(z, P_z, Q^2) = A_1 = \frac{2\sqrt{E_0^i E_0^f}}{E_0^i + E_0^f} F^t = F^B. \tag{8}$$

Our subsequent calculations will focus on matrix elements of the time component within the non-Breit frame as the most computationally efficient.

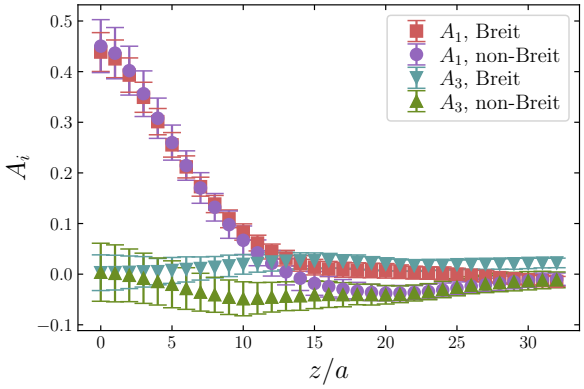

Figure 1: The results of the amplitudes $A_i(i = 1, 3)$ solved from both the Breit and non-Breit frames are shown.

4. Valence GPD

Since we aim to get results for pion GPD within the LaMET framework, we selected the two largest momenta available for the calculation in the non-Breit frame. For each momentum, we analyzed six values of the momentum transfer Q^2. Fig. 2 illustrates the bare matrix elements results for the largest momentum, $|\mathbf{P}^f| = P_z = 1.937$ GeV, depicted as a function of the Wilson-line length, z. These bare matrix elements display a decreasing trend as the length of the Wilson line increases and also as the momentum transfer increases, as expected. Several steps are required to derive the qGPD from the bare matrix elements, including renormalization, extrapolation, and Fourier transform. Subsequently, we use LaMET to get the valence GPD from the quasi-GPD.

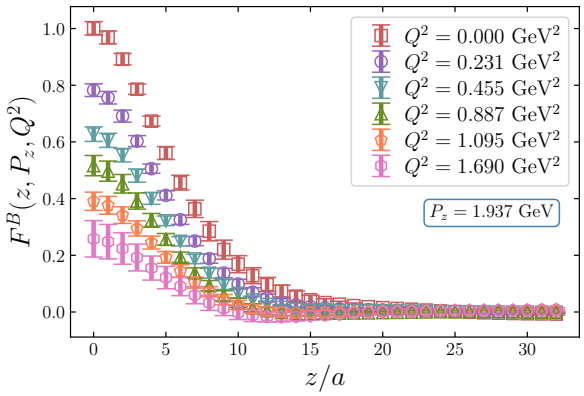

Figure 2: The bare matrix element results of the largest momentum $|\mathbf{P}^f| = P_z = 1.937$ GeV are shown. The various symbols represent outcomes corresponding to distinct momenta transfer Q^2.

4.1 Hybrid-scheme renormalization

The renormalization is crucial for removing the UV divergences from the Wilson line. Commonly employed renormalization methods include Regularization-Independent Momentum-subtraction (RI-MOM) [27–30] and various ratio schemes [31–35]. However, these methods adhere

to a factorization relation with the light-cone correlation only at short distances. At long distances, they introduce non-perturbative effects [36], which will impact the qGPD through the Fourier transform of the matrix elements, thereby affecting the LaMET matching results in x-space. To overcome this issue, a hybrid-scheme renormalization has been developed [36], which can eliminate linear divergence at long distances without introducing additional non-perturbative effects.

It is important to note that the insertion operator is multiplicative, allowing the relation between the bare and renormalized matrix elements to be expressed as [37–39]

$$F^B(z,a) = Z(a)e^{-\delta m(a)|z|}e^{-\bar{m}_0|z|}F^R(z,a), \tag{9}$$

where the superscripts B and R denote the bare and renormalized quantities, respectively, $Z(a)$ includes the logarithmic divergence which is z-independent, the term with $\delta m(a)$ accounts for the linear divergence, and the term with $\bar{m}_0$ is introduced to handle the renormalon ambiguity induced by the scheme-dependence of δm and match the lattice scheme to $\overline{\text{MS}}$ scheme [40].

The hybrid scheme renormalization is defined by merging the ratio scheme for short distances with the explicit subtraction of self-energy divergences in the Wilson line for long distances.

$$F^R(z,z_S;P_z,Q^2) = \begin{cases} \dfrac{F^B(z,P_z,Q^2)}{F^B(z,0,0)}, & z \le z_S; \\ \dfrac{F^B(z,P_z,Q^2)}{F^B(z_S,0,0)}e^{(\delta m+\bar{m}_0)|z-z_S|}, & z > z_S, \end{cases} \tag{10}$$

The segment position is denoted as z_S. In order to further mitigate the correlations and enhance the signal quality, a double ratio is employed through $F^R(z,z_S;P_z,Q^2)/F^R(0,z_S;P_z,Q^2)$, which needs to be corrected in the final results. At short distances, all the divergences can be canceled by the ratio. However, for long distances, before performing the renormalization, we need first to determine the values of δ_m and $\bar{m}_0$. To estimate δ_m, we could use lattice QCD results on the static quark-antiquark potential and the free energy of a static quark at non-zero temperatures [41], which results in $a\delta m = 0.1508(12)$ for $a = 0.04$ fm lattice [40]. The $\bar{m}_0$ value can be obtained using the bare matrix elements with zero momentum and zero momentum transfer. By comparing lattice computations with the corresponding OPE expressions for such a ratio

$$e^{(\delta m+\bar{m}_0)\Delta z}\frac{F^B(z+\Delta z)}{F^B(z)} = \frac{C_0(\alpha_s(\mu),\mu^2(z+\Delta z)^2)}{C_0(\alpha_s(\mu),\mu^2 z^2)}, \tag{11}$$

we can obtain the value of $\bar{m}_0$. For this analysis, we set the parameters to $\Delta z/a = 1$ and $\mu = 2$ GeV. Our study employs Wilson coefficients C_0 computed up to NNLO [34, 42]. Furthermore, we incorporate leading-renormalon resummation (LRR) [43, 44] into the coefficients to improve the perturbative convergence.

Fig. 3 displays the results of $\bar{m}_0$ obtained with NLO+LRR and NNLO+LRR perturbative coefficients. Theoretically, the parameter $\bar{m}_0$ should be a constant. It is observed that the NNLO results for m_0 show milder z-dependence compared to the NLO results. In the following, we adopt the $\bar{m}_0$ values at $z = 0.12$ fm in the hybrid-scheme renormalization.

In Fig. 4, we present our results for renormalized matrix elements, denoted by red square symbols, as a function of $\lambda = zP_z$. Due to the weakening of signal quality and the effect of

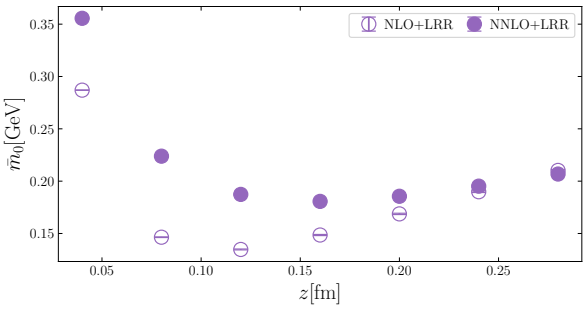

Figure 3: The results of $\bar{m}_0$ obtained with NLO+LRR (denoted as the open symbols) and NNLO+LRR (denoted as the filled symbols) Wilson coefficients are shown.

finite volume, we can only calculate the renormalized matrix element up to some maximal value of λ. This will lead to unphysical oscillations in the qGPD results. To address this problem, we extrapolate the data from a certain cutoff point to a sufficiently large distance. The extrapolation employs an exponential decay model, expressed as $Ae^{-m_{\text{eff}}z}/\lambda^d$, where A, m_{eff}, and d are the fit parameters. The extrapolated results, indicated by purple circle symbols in Fig. 4, exhibit desirable decay behavior at long distances and start to approach zero from a sufficiently large distance.

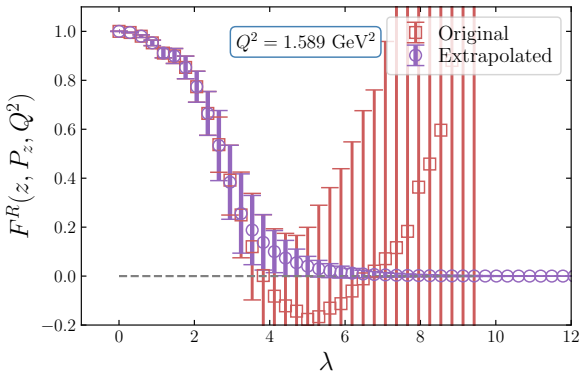

Figure 4: The renormalized matrix elements (indicated by red square symbols), along with their extrapolated results (denoted as purple circle symbols), are presented.

4.2 From quasi-GPD to light-cone GPD

The qGPD is obtained by applying the Fourier transform to the extrapolated results after renormalization.

$$\tilde{f}(x, p_z, Q^2) = \int \frac{\mathrm{d}\lambda}{2\pi} e^{ix\lambda} F^R(z, p_z, Q^2). \tag{12}$$

We employ the LaMET approach for the perturbative matching of qGPD to the valence GPD in the light-cone framework.

$$f(x, Q^2) = \int_{-\infty}^{\infty} \frac{\mathrm{d}y}{|y|} C^{-1}\left(\frac{x}{y}, \frac{\mu}{yP_z}, |y|\lambda_S\right) \tilde{f}(y, P_z, Q^2) + O\left(\frac{\Lambda^2_{\text{QCD}}}{(xP_z)^2}, \frac{\Lambda^2_{\text{QCD}}}{[(1-x)P_z]^2}\right), \tag{13}$$

where $\lambda_S = z_S P_z$ with $z_S = 0.12$ fm, and C^{-1} represents the inverse of the matching coefficient. Fig. 5 displays the valence GPD results of the largest momentum as a function of Bjorken-x across all momentum transfer values. The GPD decreases with the momentum transfer increases, and its x-dependence becomes weaker with increasing value of Q^2, except for very small values of x.

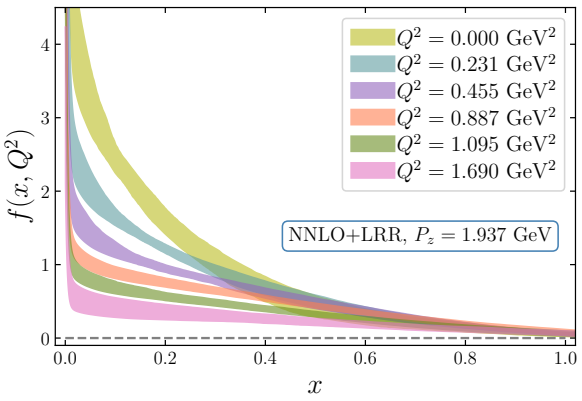

Figure 5: The results of the valence GPD for $P_z = 1.937$ GeV are shown, spanning a range of varying momentum transfer Q^2.

The P_z- and x-dependence of the valence GPD are illustrated in Fig. 6. The left panel presents the distributions for two similar momentum transfer values $Q^2 = 0.229, 0.231$ GeV^2, from $P_z = 1.45, 1.94$ GeV, respectively. Among the qGPD results, represented as bands filled with lines, considerable discrepancies are observed between results with similar Q^2 values but different P_z values. Notably, the perturbative matching results, denoted as the bands filled with colors, effectively correct these differences. This not only underscores the validity of the results but also highlights the efficacy of the LaMET approach. In the right panel, the distributions are shown for five distinct x values as a function of the momentum transfer. We see that for small values of x, the pion GPD shows significant Q^2 dependence. However, for large values of x, the Q^2-dependence of the GPD becomes mild. This means that valance quarks at large values of x have a very narrow distribution in the transverse size.

5. Generalized Form Factor

We use leading twist OPE to obtain GFF. Since this involves only small values of z we renormalize the matrix elements with the ratio scheme and then combine the lattice data with the leading-twist OPE approximation by such a formula

$$F^R(z, P_z, Q^2) = \sum_{n=0} \frac{(-izP_z)^n}{n!} \frac{C_n(\mu^2 z^2)}{C_0(\mu^2 z^2)} \langle x^n \rangle + O(\Lambda^2_{\rm QCD} z^2), \tag{14}$$

where the Wilson coefficients are calculated up to NNLO and $\langle x^n \rangle$ denotes the Mellin moments with $n \in [0, 2, 4]$, defined as

$$\langle x^n \rangle = \int_{-1}^{1} x^n f(x, \xi = 0, Q^2) \mathrm{d}x = A_{n+1, \xi=0}(Q^2), \tag{15}$$

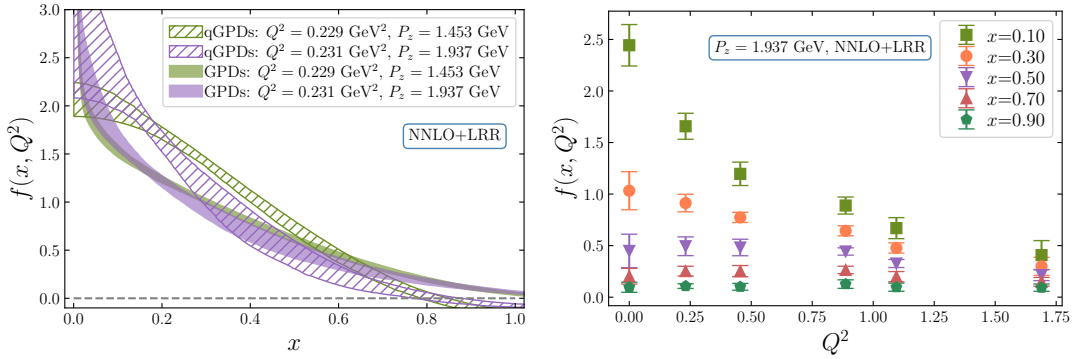

Figure 6: The valence GPD obtained with NNLO+LRR matching are shown. Left: P_z-dependence is displayed by comparing the results of two datasets with similar momentum transfer before and after perturbative matching. The quasi-GPD results are presented by bands filled with lines, while the light-cone GPD results are depicted using bands filled with colors. Right: To explore the Q^2-dependence, we select five distinct values of Bjorken-x and display the distributions as a function of Q^2.

where $A_{n+1,\xi=0}(Q^2)$ denotes the generalized form factor (GFF). We show the results of the first three iso-vector GFFs results obtained within scale $\mu = 2$ GeV in Fig. 7. The results demonstrate a power law decay behavior as the momentum transfer increases. It is essential to emphasize that the first GFF, denoted as $A_{1,0}$, corresponds to the electromagnetic form factor (EMFF). And our findings align well with the EMFF results reported by the ETM collaboration [45], represented as the blue line in the figure. Regarding the results for $A_{3,0}$, our results also exhibit consistency with other lattice studies [13, 46–48] within a 1-σ margin of error. Notably, we initially investigate the variation of the pion's fifth GFF, $A_{5,0}$, with respect to Q^2.

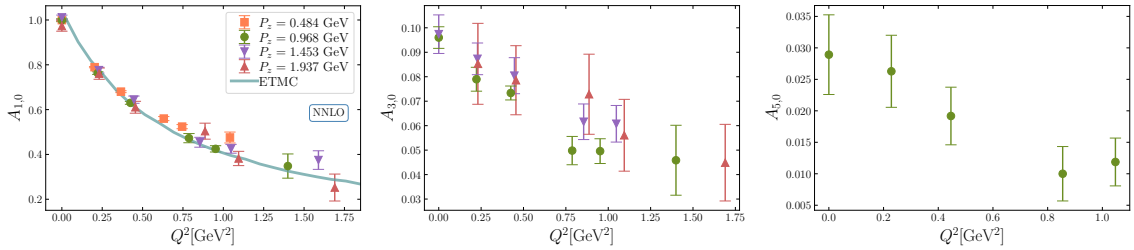

Figure 7: From left to right, the results of the first three iso-vector GFFs, namely $A_{1,0}$, $A_{3,0}$ and $A_{5,0}$, as a function of Q^2 are shown.

6. Conclusion and Outlook

Based on the Lorentz-covariant parameterization of the matrix elements, we extracted amplitudes from both the Breit and non-Breit frames at similar momentum transfer values, confirming their frame-independent property. This verification allows us to perform lattice GPD calculations without frame restriction. Focusing on the large momentum cases within the asymmetric frame, we obtained valence GPD results with hybrid-scheme renormalization and the LaMET framework. We incorporated Wilson coefficients up to NNLO in conjunction with LRR. We studied the dependent

behavior of valence GPD results from various perspectives. Additionally, by concentrating on short distances, we utilized the ratio-scheme renormalized data to derive the first three iso-vector GFFs, applying the leading-twist factorization formula with matching coefficients up to NNLO.

Regarding future work on valance GPD, we intend to integrate DGLAP evolution to deepen our understanding of scale variation behavior. For the GFF, we aim to extend acquiring additional moments and more accurate results.

7. Acknowledgments

We thank Shohini Bhattacharya, Yushan Su, and Rui Zhang for their valuable communications. This material is based upon work supported by The U.S. Department of Energy, Office of Science, Office of Nuclear Physics through Contract Nos. DE-SC0012704, DE-AC02-06CH11357, and within the frameworks of Scientific Discovery through Advanced Computing (SciDAC) award Fundamental Nuclear Physics at the Exascale and Beyond, and under the umbrella of the Quark-Gluon Tomography (QGT) Topical Collaboration with Award DE-SC0023646. SS is supported by the National Science Foundation under CAREER Award PHY-1847893 and by the RHIC Physics Fellow Program of the RIKEN BNL Research Center. YZ is partially supported by the 2023 Physical Sciences and Engineering (PSE) Early Investigator Named Award program at Argonne National Laboratory. HTD is partially supported by the National Natural Science Foundation of China under Grants No. 12293064, No. 12293060 and No. 12325508.

This research used awards of computer time provided by the U.S. Department of Energy's INCITE and ALCC programs at the Argonne and the Oak Ridge Leadership Computing Facilities. The Argonne Leadership Computing Facility at Argonne National Laboratory is supported by the Office of Science of the U.S. DOE under Contract No. DE-AC02-06CH11357. The Oak Ridge Leadership Computing Facility at the Oak Ridge National Laboratory is supported by the Office of Science of the U.S. DOE under Contract No. DE-AC05-00OR22725. Computations for this work were carried out in part on facilities of the USQCD Collaboration, funded by the Office of Science of the U.S. Department of Energy, and the Nuclear Science Computing Center at Central China Normal University (NSC^3) and Wuhan Supercomputing Center.

References

[1] S. R. Amendolia et al. (NA7), Nucl. Phys. B **277**, 168 (1986).

[2] J. S. Conway et al., Phys. Rev. D **39**, 92 (1989).

[3] D. Müller, D. Robaschik, B. Geyer, F. M. Dittes, and J. Hořejši, Fortsch. Phys. **42**, 101 (1994), arXiv:hep-ph/9812448 .

[4] X.-D. Ji, Phys. Rev. Lett. **78**, 610 (1997), arXiv:hep-ph/9603249 .

[5] A. V. Radyushkin, Phys. Lett. B **380**, 417 (1996), arXiv:hep-ph/9604317 .

[6] X.-D. Ji, Phys. Rev. D **55**, 7114 (1997), arXiv:hep-ph/9609381 .

[7] J. Dudek et al., Eur. Phys. J. A **48**, 187 (2012), arXiv:1208.1244 [hep-ex] .

[8] B. Adams et al., (2018), arXiv:1808.00848 [hep-ex] .

[9] R. Abdul Khalek et al., Nucl. Phys. A **1026**, 122447 (2022), arXiv:2103.05419 [physics.ins-det] .

[10] D. P. Anderle et al., Front. Phys. (Beijing) **16**, 64701 (2021), arXiv:2102.09222 [nucl-ex] .

[11] X. Ji, Phys. Rev. Lett. **110**, 262002 (2013), arXiv:1305.1539 [hep-ph] .

[12] X. Ji, Y.-S. Liu, Y. Liu, J.-H. Zhang, and Y. Zhao, Rev. Mod. Phys. **93**, 035005 (2021), arXiv:2004.03543 [hep-ph] .

[13] H.-W. Lin, Phys. Lett. B **846**, 138181 (2023), arXiv:2310.10579 [hep-lat] .

[14] J.-W. Chen, H.-W. Lin, and J.-H. Zhang, Nucl. Phys. B **952**, 114940 (2020), arXiv:1904.12376 [hep-lat] .

[15] S. Bhattacharya, K. Cichy, M. Constantinou, J. Dodson, X. Gao, A. Metz, S. Mukherjee, A. Scapellato, F. Steffens, and Y. Zhao, Phys. Rev. D **106**, 114512 (2022), arXiv:2209.05373 [hep-lat] .

[16] A. Bazavov et al., Phys. Rev. D **100**, 094510 (2019), arXiv:1908.09552 [hep-lat] .

[17] E. Follana, Q. Mason, C. Davies, K. Hornbostel, G. P. Lepage, J. Shigemitsu, H. Trottier, and K. Wong (HPQCD, UKQCD), Phys. Rev. D **75**, 054502 (2007), arXiv:hep-lat/0610092 .

[18] A. Hasenfratz and F. Knechtli, Phys. Rev. D **64**, 034504 (2001), arXiv:hep-lat/0103029 .

[19] X. Gao, L. Jin, C. Kallidonis, N. Karthik, S. Mukherjee, P. Petreczky, C. Shugert, S. Syritsyn, and Y. Zhao, Phys. Rev. D **102**, 094513 (2020), arXiv:2007.06590 [hep-lat] .

[20] G. S. Bali, B. Lang, B. U. Musch, and A. Schäfer, Phys. Rev. D **93**, 094515 (2016), arXiv:1602.05525 [hep-lat] .

[21] J. Brannick, R. C. Brower, M. A. Clark, J. C. Osborn, and C. Rebbi, Phys. Rev. Lett. **100**, 041601 (2008), arXiv:0707.4018 [hep-lat] .

[22] M. A. Clark, R. Babich, K. Barros, R. C. Brower, and C. Rebbi (QUDA), Comput. Phys. Commun. **181**, 1517 (2010), arXiv:0911.3191 [hep-lat] .

[23] R. Babich, M. A. Clark, B. Joo, G. Shi, R. C. Brower, and S. Gottlieb (QUDA), in International Conference for High Performance Computing, Networking, Storage and Analysis (2011) arXiv:1109.2935 [hep-lat] .

[24] M. A. Clark, B. Joó, A. Strelchenko, M. Cheng, A. Gambhir, and R. C. Brower (QUDA), in International Conference for High Performance Computing, Networking, Storage and Analysis (2016) arXiv:1612.07873 [hep-lat] .

[25] T. Izubuchi, L. Jin, C. Kallidonis, N. Karthik, S. Mukherjee, P. Petreczky, C. Shugert, and S. Syritsyn, Phys. Rev. D **100**, 034516 (2019), arXiv:1905.06349 [hep-lat] .

[26] E. Shintani, R. Arthur, T. Blum, T. Izubuchi, C. Jung, and C. Lehner, Phys. Rev. D **91**, 114511 (2015), arXiv:1402.0244 [hep-lat] .

[27] M. Constantinou and H. Panagopoulos, Phys. Rev. D **96**, 054506 (2017), arXiv:1705.11193 [hep-lat] .

[28] C. Alexandrou, K. Cichy, M. Constantinou, K. Hadjiyiannakou, K. Jansen, H. Panagopoulos, and F. Steffens, Nucl. Phys. B **923**, 394 (2017), arXiv:1706.00265 [hep-lat] .

[29] I. W. Stewart and Y. Zhao, Phys. Rev. D **97**, 054512 (2018), arXiv:1709.04933 [hep-ph] .

[30] J.-W. Chen, T. Ishikawa, L. Jin, H.-W. Lin, Y.-B. Yang, J.-H. Zhang, and Y. Zhao, Phys. Rev. D **97**, 014505 (2018), arXiv:1706.01295 [hep-lat] .

[31] A. V. Radyushkin, Phys. Rev. D **96**, 034025 (2017), arXiv:1705.01488 [hep-ph] .

[32] K. Orginos, A. Radyushkin, J. Karpie, and S. Zafeiropoulos, Phys. Rev. D **96**, 094503 (2017), arXiv:1706.05373 [hep-ph] .

[33] V. M. Braun, A. Vladimirov, and J.-H. Zhang, Phys. Rev. D **99**, 014013 (2019), arXiv:1810.00048 [hep-ph] .

[34] Z.-Y. Li, Y.-Q. Ma, and J.-W. Qiu, Phys. Rev. Lett. **126**, 072001 (2021), arXiv:2006.12370 [hep-ph] .

[35] Z. Fan, X. Gao, R. Li, H.-W. Lin, N. Karthik, S. Mukherjee, P. Petreczky, S. Syritsyn, Y.-B. Yang, and R. Zhang, Phys. Rev. D **102**, 074504 (2020), arXiv:2005.12015 [hep-lat] .

[36] X. Ji, Y. Liu, A. Schäfer, W. Wang, Y.-B. Yang, J.-H. Zhang, and Y. Zhao, Nucl. Phys. B **964**, 115311 (2021), arXiv:2008.03886 [hep-ph] .

[37] X. Ji, J.-H. Zhang, and Y. Zhao, Phys. Rev. Lett. **120**, 112001 (2018), arXiv:1706.08962 [hep-ph] .

[38] T. Ishikawa, Y.-Q. Ma, J.-W. Qiu, and S. Yoshida, Phys. Rev. D **96**, 094019 (2017), arXiv:1707.03107 [hep-ph] .

[39] J. Green, K. Jansen, and F. Steffens, Phys. Rev. Lett. **121**, 022004 (2018), arXiv:1707.07152 [hep-lat] .

[40] X. Gao, A. D. Hanlon, S. Mukherjee, P. Petreczky, P. Scior, S. Syritsyn, and Y. Zhao, Phys. Rev. Lett. **128**, 142003 (2022), arXiv:2112.02208 [hep-lat] .

[41] A. Bazavov, N. Brambilla, P. Petreczky, A. Vairo, and J. H. Weber (TUMQCD), Phys. Rev. D **98**, 054511 (2018), arXiv:1804.10600 [hep-lat] .

[42] L.-B. Chen, W. Wang, and R. Zhu, Phys. Rev. Lett. **126**, 072002 (2021), arXiv:2006.14825 [hep-ph] .

[43] J. Holligan, X. Ji, H.-W. Lin, Y. Su, and R. Zhang, Nucl. Phys. B **993**, 116282 (2023), arXiv:2301.10372 [hep-lat] .

[44] R. Zhang, J. Holligan, X. Ji, and Y. Su, Phys. Lett. B **844**, 138081 (2023), arXiv:2305.05212 [hep-lat] .

[45] C. Alexandrou, S. Bacchio, I. Cloet, M. Constantinou, J. Delmar, K. Hadjiyiannakou, G. Koutsou, C. Lauer, and A. Vaquero (ETM), Phys. Rev. D **105**, 054502 (2022), arXiv:2111.08135 [hep-lat] .

[46] M. Oehm, C. Alexandrou, M. Constantinou, K. Jansen, G. Koutsou, B. Kostrzewa, F. Steffens, C. Urbach, and S. Zafeiropoulos, Phys. Rev. D **99**, 014508 (2019), arXiv:1810.09743 [hep-lat] .

[47] C. Alexandrou, S. Bacchio, I. Cloet, M. Constantinou, K. Hadjiyiannakou, G. Koutsou, and C. Lauer (ETM), Phys. Rev. D **103**, 014508 (2021), arXiv:2010.03495 [hep-lat] .

[48] X. Gao, A. D. Hanlon, N. Karthik, S. Mukherjee, P. Petreczky, P. Scior, S. Shi, S. Syritsyn, Y. Zhao, and K. Zhou, Phys. Rev. D **106**, 114510 (2022), arXiv:2208.02297 [hep-lat] .